Comparison of the ocean inherent optical properties obtained from measurements and inverse modeling

Hubert Loisel, Dariusz Stramski, B. Greg Mitchell, Frank Fell, Vincent Fournier-Sicre, Bertand Lemasle, and Marcel Babin

A model developed recently by Loisel and Stramski [Appl. Opt. **39,** 3001–3011 (2000)] for estimating the spectral absorption $a(\lambda)$, scattering $b(\lambda)$, and backscattering $b_b(\lambda)$ coefficients in the upper ocean from the irradiance reflectance just beneath the sea surface $R(\lambda, z = 0^-)$ and the diffuse attenuation of downwelling irradiance within the surface layer $\langle K_d(\lambda)\rangle_1$ is compared with measurements. Field data for this comparison were collected in different areas including off-shore and near-shore waters off southern California and around Europe. The $a(\lambda)$ and $b_b(\lambda)$ values predicted by the model in the blue-green spectral region show generally good agreement with measurements that covered a broad range of conditions from clear oligotrophic waters to turbid coastal waters affected by river discharge. The agreement is still good if the model estimates of $a(\lambda)$ and $b_b(\lambda)$ are based on $R(\lambda, z = 0^-)$ used as the only input to the model available from measurements [as opposed to both $R(\lambda, z = 0^-)$ and $\langle K_d(\lambda)\rangle_1$ being measured]. This particular mode of operation of the model is relevant to ocean-color remote-sensing applications. In contrast to $a(\lambda)$ and $b_b(\lambda)$ the comparison between the modeled and the measured $b(\lambda)$ shows large discrepancies. These discrepancies are most likely attributable to significant variations in the scattering phase function of suspended particulate matter, which were not included in the development of the model.

OCIS codes: 010.4450, 030.5620, 290.5860, 280.0280.

1. Introduction

Inherent optical properties (IOP's) such as spectral absorption $a(\lambda)$, scattering $b(\lambda)$, and backscattering $b_b(\lambda)$ coefficients are essential for characterizing the marine optical environment and remote-sensing applications. In recent years significant effort has been devoted to the development of models for estimating IOP's from underwater light-field measurements and apparent optical properties (AOPs).[1–8] The AOPs commonly used in these models include the diffuse attenuation coefficient for downwelling irradiance $K_d(\lambda)$, irradiance reflectance $R(\lambda)$, and remote-sensing reflectance $R_{rs}(\lambda)$ (see Table 1 for symbols and definitions). These models are based on certain assumptions and methods that could limit their potential application. For example, the models involve assumptions about the spectral behavior of IOPs (see, e.g., Refs. 4, 6, and 7), require input data from measurements at different Sun angles (see, e.g., Ref. 2), or are relatively complex methods for solving the problem by use of input data that characterize the vertical profiles of the underwater light-field characteristics[9] and iterative radiative-transfer simulations.[5,10]

To overcome these limitations, we recently developed a simple inverse model for retrieving $a(\lambda)$, $b(\lambda)$, and $b_b(\lambda)$ within the surface ocean layer from two basic AOPs.[1] These AOPs are the irradiance reflectance just beneath the sea surface $R(\lambda, z = 0^-)$ and the average attenuation coefficient for downwelling irradiance $\langle K_d(\lambda)\rangle_1$ between the sea surface and the first attenuation depth z_1 at which the downwelling irradiance $E_d(\lambda)$ is reduced to 37% of its surface value (note that z_1 is a function of λ). Our model can be

When this research was performed, H. Loisel and D. Stramski were with the Marine Physical Laboratory, Scripps Institution of Oceanography, University of California at San Diego, La Jolla, California 92093-0238. H. Loisel (loisel@loa.univ-lillel.fr) is now with the Laboratoire d'Optique Atmospherique, Université de Lille 1, F-59655 Villeneuve d'Ascq Cedex, France. B. G. Mitchell is with the Marine Research Division, Scripps Institution of Oceanography, University of California at San Diego, La Jolla, California 92093-0218. F. Fell, B. Lemasle, and M. Babin are with the Laboratoire de Physique et Chimie Marines, B.P. 08, F06238 Villefranche sur Mer Cedex, France. V. Fournier-Sicre is with ACRI, 260 route du Pin Montard, B.P. 234, 06904 Sophia Antipolis Cedex, France.

Received 17 July 2000; revised manuscript received 30 January 2001.

0003-6935/01/152384-14$15.00/0

Table 1. Notation

Symbol	Definition	Unit
a	Total absorption coefficient	m^{-1}
a_w	Pure water absorption coefficient	m^{-1}
a_p	Particle absorption coefficient	m^{-1}
a_s	Soluble organic matter absorption coefficient	m^{-1}
b	Total scattering coefficient	m^{-1}
b_w	Pure water scattering coefficient	m^{-1}
b_p	Particle scattering coefficient	m^{-1}
c	Beam attenuation coefficient ($= a + b$)	m^{-1}
b_b	Total backscattering coefficient	m^{-1}
b_{bw}	Pure water backscattering coefficient	m^{-1}
b_{bp}	Particle backscattering coefficient	m^{-1}
η	Ratio of molecular scattering to total scattering ($= b_w/b$)	
θ_0	Solar zenith angle in air	
θ_v	Viewing zenith angle in air	
ϕ_v	Viewing azimuth angle in air	
μ_w	Cosine of solar zenith angle in water	
λ	Light wavelength in vacuum	nm
z	Geometric depth	m
z_1	First attenuation depth	m
Chl	Chlorophyll concentration	$mg\ m^{-3}$
E_u	Upwelling irradiance on a horizontal surface	$W\ m^{-2}$
E_d	Downwelling irradiance on a horizontal surface	$W\ m^{-2}$
K_d	Vertical attenuation coefficient for E_d ($= -\mathrm{d} \ln E_d/\mathrm{d}z$)	m^{-1}
$\langle K_d \rangle_1$	Average K_d within the layer between the surface and z_1	m^{-1}
R	Irradiance reflectance ($= E_u/E_d$)	
R^e	Irradiance reflectance in the absence of Raman scattering	
R_{rs}	Remote-sensing reflectance	sr^{-1}
L_{wn}	Normalized water-leaving radiance	sr^{-1}
L_u	In-water upwelling radiance	$Wm^{-2}\ sr^{-1}$
Q	Ratio of the upwelling irradiance to the upwelling radiance ($= E_u/L_u$)	sr

applied to measurements taken at any solar zenith angle θ_0. The model accounts for the effect of Raman scattering, and thus it can be applied to various wavelengths in the visible spectrum, perhaps with the exception of wave bands where strong fluorescence of biogenic material occurs, for example, near 680 nm in waters with high chlorophyll concentration. More important, the model is also independent of the spectral shape of the IOPs. Therefore it provides a suitable tool for testing consistency between *in situ* measurements of IOPs and radiometric quantities of the light field. In addition, the model can be applied to remote-sensing ocean-color data.

The model was previously tested with numerical simulations of radiative transfer by use of IOPs that were assumed to be inputs to these simulations. Development of commercial instrumentation in recent years has provided a capability to determine IOPs routinely from *in situ* measurements. Spectral absorption $a(\lambda)$ and beam attenuation $c(\lambda)$ coefficients are routinely collected with absorption-attenuation meters such as ac-9 (WET Labs, Inc.).[7,11–14] From these data the scattering coefficient $b(\lambda)$ is derived simply as the difference between $c(\lambda)$ and $a(\lambda)$. The backscattering coefficient $b_b(\lambda)$ can also be estimated from *in situ* measurements with backscattering sensors such as Hydroscat-6 (HOBI Labs, see e.g., Ref. 15).

The objective of this study is to examine closure between data from *in situ* measurements of IOPs, that is, $a(\lambda)$, $b(\lambda)$, and $b_b(\lambda)$, and the retrieval of these coefficients from our model based on concurrent measurements of $R(\lambda, z = 0^-)$ and $\langle K_d(\lambda) \rangle_1$. We begin with a brief description of field measurements and an overview of the model. Because the model was originally developed with radiative-transfer simulations for a vertically homogeneous water column, we present a sensitivity analysis for several situations of depth-dependent IOPs. We then compare the model retrievals with IOP measurements made in various oceanic areas, which include both off-shore and coastal environments. Finally, a similar closure analysis is performed within the context of ocean-color remote-sensing application where $\langle K_d(\lambda) \rangle_1$ values were estimated from $R(\lambda, z = 0^-)$ rather than from direct measurement.

2. Field Measurements

The field data were collected off southern California as part of the California Cooperative Oceanic Fisheries Investigations[16] (CalCOFI) and in waters surrounding Europe as part of the Coastal Surveillance through Observation of Ocean Color (COASTlOOC) project. For our analysis we selected the CalCOFI data that were taken at 11 stations during cruises in July and September 1998. These stations represent both near-shore and off-shore locations with significant differences in ocean optical properties. For the

COASTlOOC project, 29 stations representing a broad range of optical water types were selected from various regions. Specifically, the data were collected in the coastal zone of the North Sea affected by the Rhine River discharge, in the open ocean west off Europe and North Africa, and in off-shore as well as near-shore waters in the proximity of the Rhône River in the Lions Gulf, Mediterranean. These data were collected during cruises in April and September–October 1997.

From the CalCOFI cruises, measurements included spectral downwelling and upwelling irradiances, $E_d(z, \lambda)$ and $E_u(z, \lambda)$, the spectral backscattering coefficient $b_b(z, \lambda)$, and the spectral absorption coefficient $a(z, \lambda)$. This data set allows us to examine the closure for $a(z, \lambda)$ and $b_b(z, \lambda)$. The methods and data-processing procedures for the AOPs were described by Mitchell and Kahru.[16] In brief, the underwater vertical profiles of $E_d(z, \lambda)$ and $E_u(z, \lambda)$ were measured with a MER-2048 spectroradiometer (Biospherical Instruments) at different wavelength bands between 340 and 665 nm. These irradiance data were used to calculate the reflectance $R(\lambda, z = 0^-)$ and the irradiance attenuation coefficient $\langle K_d(\lambda)\rangle_1$, which are needed as input to our model. In our analysis we use the data at six wave bands centered at 412, 443, 490, 510, 555, and 665 nm for which measurements of both $E_d(z, \lambda)$ and $E_u(z, \lambda)$ were available. The backscattering coefficient $b_b(z, \lambda)$ was determined from measurements with a Hydroscat-6 sensor (HOBI Labs) at six wavelengths, 442, 488, 532, 589, 620, and 671 nm. A power function of λ was fitted to each set of spectral values of $b_b(z, \lambda)$. The estimates of $b_b(z, \lambda)$ provided by these fits at wavelengths matching the five wave bands of MER-2048 will be used in the analysis of closure between the measured and the modeled backscattering coefficient.

The absorption spectra $a(z, \lambda)$ were determined as a sum of contributions by pure seawater,[17] particles, and soluble materials. The absorption by particles and soluble materials was measured during the CalCOFI cruises on water samples taken from discrete depths with the ship's conductivity–temperature–depth rosette by use of onboard double-beam spectrophotometer. This measurement provided data from 300 to 750 nm at 2-nm intervals. The particulate absorption spectra $a_p(z, \lambda)$ were determined with a filter-pad technique.[18] The absorption by soluble matter $a_s(z, \lambda)$ was measured in a 10-cm quartz cuvette on samples filtered through prerinsed 0.2-μm Nuclepore filters with Milli-Q water as reference.[19] Water samples were usually taken shortly before or after the optical casts, but occasionally these events were separated by more than 1 h. The analysis of closure for the absorption coefficient will include the six MER-2048 wave bands.

The COASTlOOC data include measurements of $E_d(z, \lambda)$, $E_u(z, \lambda)$, $a(z, \lambda)$, and $c(z, \lambda)$, which also provided the scattering coefficient $b(z, \lambda)$. Thus this data set allows us to examine the closure between the measured and the modeled IOPs for $a(z, \lambda)$ and $b(z, \lambda)$. The COASTlOOC measurements were made with an *in situ* optical system that included a Sea-viewing Wide Field-of-view Sensor (Sea WiFS) profiling multichannel radiometer (SPMR) (Satlantic) and an ac-9 instrument (WET Labs, Inc.). The SPMR instrument measured $E_d(z, \lambda)$ and $E_u(z, \lambda)$ at 15 spectral bands between 411 and 865 nm, and an ac-9 meter provided $a(z, \lambda)$ and $c(z, \lambda)$ at nine wavelengths between 412 and 715 nm. The closure analysis for a and b for the COASTlOOC data will include five wavelengths, for which there is a good match between the ac-9 and SPMR bands, that is, 412, 440, 488, 510, and 555 nm.

3. Overview of the Model

Our model is based on two distinct sets of numerical simulations of radiative transfer in the ocean, which are described in detail by Loisel and Stramski.[1] Although the first set of simulations was made with no Raman scattering by water, the second set includes this inelastic scattering process. The results from simulations in the absence of Raman scattering were used to establish basic equations of the model, which relate the IOPs to irradiance reflectance $R^e(z = 0^-)$ and the attenuation coefficient $\langle K_d\rangle_1$. The superscript e indicates that the variable was obtained under the assumption that only elastic scattering occurs, that is, there is no Raman scattering by water. (Note that fluorescence processes were ignored in the model development.) This subscript is omitted for $\langle K_d\rangle_1$ because the effect of Raman scattering on this quantity is small (see, e.g., Ref. 1). The basic equations are

$$a = \frac{\mu_w \langle K_d\rangle_1}{\left[1 + (2.54 - 6.54\mu_w + 19.89\mu_w^2)\dfrac{R^e(0^-)}{1 - R^e(0^-)}\right]^{0.5}}, \quad (1)$$

where μ_w is the cosine of the refracted solar beam angle just beneath the surface,

$$b = \frac{a\dfrac{R^e(0^-)}{1 - R^e(0^-)} - b_w(0.165 - 0.0358\mu_w)}{0.0215 - 0.0149\mu_w}, \quad (2)$$

where b_w is the scattering coefficient that is due to water molecules, and

$$b_b = \langle K_d\rangle_1 10^{\alpha}[R^e(0^-)]^{\delta}. \quad (3)$$

The α and δ functions are described as

$$\alpha = (-0.83 + 5.34\eta - 12.26\eta^2) + \mu_w(1.013 - 4.124\eta + 8.088\eta^2), \quad (4)$$

$$\delta = 0.871 + 0.40\eta - 1.83\eta^2, \quad (5)$$

where η $(= b_w/b)$ is the ratio of molecular scattering to total scattering. Equations (1)–(5) can be applied at any wavelength λ within the visible spectrum.

The second set of simulations allowed us to assess the contribution of Raman scattering to the actual

reflectance $R(z = 0^-)$. This reflectance represents the actual situations in the ocean when both elastic scattering and Raman scattering are present. We developed an iterative scheme for calculating $R^e(z = 0^-)$ from $R(z = 0^-)$, because it is the hypothetical reflectance in the absence of Raman scattering $R^e(z = 0^-)$ rather than the actual or measured reflectance $R(z = 0^-)$ that is used as input in the final Eqs. (1)–(3) of our model.

Our previous tests based on numerical simulations over a broad range of IOPs and a Sun zenith angle of $\leq 60°$ showed the maximal errors in the retrieval of a, b, and b_b to be 6.5%, 23%, and 20%, respectively.[1] The best estimation for a and b_b was obtained in the blue and the green parts of the spectrum, where the errors ranged from a few percent to less than 10%.

4. Sensitivity to the Vertical Structure of Inherent Optical Properties

Our model was originally developed for an optically homogeneous water column. To test the sensitivity of the model to the vertical structure of the IOPs, we made numerical simulations with the Hydrolight 4.0 radiative-transfer code[20] in a similar way as described by Loisel and Stramski.[1] One major difference is that the IOPs in the present simulations vary with depth. We used the concentration of chlorophyll a (Chl) as a basis for generating the vertical structure of IOPs. Specifically, we used the depth profiles of Chl, which have the form of the Gaussian distribution.[21]

$$Chl(z) = Chl_0 + \frac{h}{\sigma(2\sigma)^{1/2}} \exp\left[-\frac{(z - z_m)^2}{2\sigma^2}\right], \quad (6)$$

where Chl_0 is the constant background for a chlorophyll a concentration, z_m is the depth of the deep chlorophyll maximum (DCM), σ is the thickness of the DCM layer, and h is the parameter that describes the total biomass above Chl_0.

By varying the parameters Chl_0, z_m, σ, and h, we have generated five profiles [Figs. 1(a) and 1(b)]. These profiles can be representative of various trophic states of the ocean, from highly productive waters, such as in the eutrophic coastal environments [Fig. 1(a)] to low biomass oligotrophic ocean waters with the DCM at 80 m [Fig. 1(b)]. One profile in Fig. 1(a) that depicts the greatest variation in Chl with depth was created arbitrarily to model dramatic changes over 2 orders of magnitude in Chl within the near-surface layer. The parameters Chl_0, z_m, σ, and h for the remaining Chl profiles are based on actual measurements of Chl in the coastal waters and open ocean taken by Platt *et al.*[22]

With these $Chl(z)$ profiles we calculated the vertical structure of IOPs in two ways. First, we used the bio-optical model of Morel and Gentili,[23] in which both the absorption and the scattering coefficients covary with Chl. This set of IOP profiles is referred to as $IOP_{ab\text{-}Chl}$. One example of these profiles for 440 nm is shown in Fig. 1(c) for one $Chl(z)$ profile. Second, the absorption coefficient profiles were calculated from $Chl(z)$ as above, but the scattering coefficient was assumed constant throughout the entire water column. The value of $b(440)$ was calculated from the relationship between $b(550)$ and Chl[24] by using the average chlorophyll concentration within the layer between the sea surface and the first attenuation depth at $\lambda = 550$ nm in conjunction with the λ^{-1} spectral dependence of b. This second set of profiles will be referred to as $IOP_{a\text{-}Chl}$ and is used in an attempt to account for the observation that the scattering coefficient is not necessarily correlated with Chl.[25] One example of these profiles at 440 nm is shown in Fig. 1(d) for the same $Chl(z)$ profile used in Fig. 1(c). In these calculations the absorption and the scattering coefficients of pure seawater were taken from Pope and Fry[17] and Morel,[26] respectively.

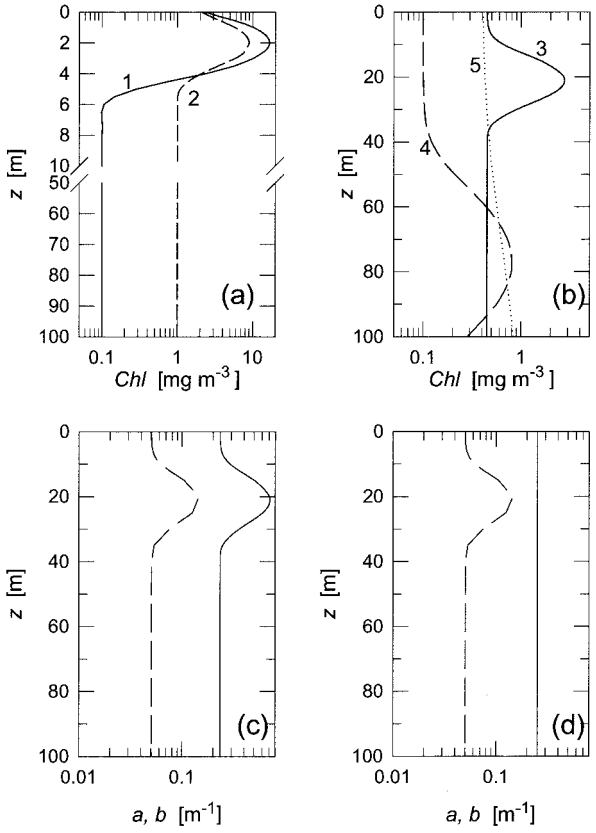

Fig. 1. (a) Vertical profiles of chlorophyll a concentration characterized by a large maximum near the ocean surface, and (b) the profiles with no maximum at all and with the significant subsurface maxima characteristic of open ocean waters. (c), (d) Vertical profiles of the absorption coefficient (dashed curves) and the scattering coefficient (solid curves) for one example profile of chlorophyll, that is, profile 3 in (b). (c) Results of calculations in the case in which both absorption and scattering covary with chlorophyll concentration; (d) results of calculations when only absorption covaries with chlorophyll (see text for details about these calculations).

The performance of our model in the presence of the vertical structure of IOPs was tested with numerical simulations by use of the Hydrolight code for each IOP profile from the $IOP_{ab\text{-}Chl}$ and $IOP_{a\text{-}Chl}$ sets. Surface-boundary conditions were described by a

semiempirical sky model provided with the Hydrolight code for clear sky with a Sun zenith angle of 30° and sea-surface roughness corresponding to a wind speed of 5 m s^{-1}. The Raman scattering was neglected, which is acceptable for such a sensitivity analysis. One scattering phase function for particles represented by the average Petzold function[27] was used in these simulations regardless of depth and wavelength. The reflectance $R(\lambda, z = 0^-)$ and the attenuation coefficient $\langle K_d(\lambda)\rangle_1$ resulting from Hydrolight simulations were then used to estimate the $a(\lambda)$, $b(\lambda)$, and $b_b(\lambda)$ coefficients from our model, Eqs. (1)–(5), at three wavelengths, 440, 550, and 660 nm. We compare these IOP estimates (referred to as the $\mathrm{IOP}_{\mathrm{model}}$) with the IOPs referred to as $\mathrm{IOP}_{\mathrm{true}}$. The $\mathrm{IOP}_{\mathrm{true}}$ values represent the depth-average values within the first attenuation layer, which were calculated from both sets of vertical profiles, that is, $\mathrm{IOP}_{ab\text{-}Chl}(z)$ and $\mathrm{IOP}_{a\text{-}Chl}(z)$.

Figure 2 shows results of this comparison in terms of the relative error:

$$\mathrm{err}(\%) = \frac{\mathrm{IOP}_{\mathrm{model}} - \mathrm{IOP}_{\mathrm{true}}}{\mathrm{IOP}_{\mathrm{true}}} \times 100. \qquad (7)$$

For typical open-ocean situations that correspond to profiles from Fig. 1(b), the vertical structure of the IOPs has a slight effect on the retrieval of $a(\lambda)$, $b(\lambda)$, and $b_b(\lambda)$ averaged over the first attenuation depth [Figs. 2(c)–2(e) and 2(h)–2(j)]. In these cases the relative errors do not exceed 15% and are similar to those reported previously by Loisel and Stramski[1] for a uniform water column. The model performs best for the retrieval of $a(\lambda)$ with the error less than 6%. In addition, the errors are similar regardless of whether we consider the $\mathrm{IOP}_{ab\text{-}Chl}$ or $\mathrm{IOP}_{a\text{-}Chl}$ profiles.

For waters that are strongly stratified near the surface [see Fig. 1(a)] the accuracy of the model retrievals is reduced [Figs. 2(a), 2(b), 2(f), and 2(g)]. Nevertheless the error for the estimation of $a(\lambda)$ remains relatively low (<15%). This analysis also indicates that the retrieval of $b(\lambda)$ and $b_b(\lambda)$ is generally more sensitive to the vertical structure of IOPs than the retrieval of absorption. The errors in the $b(\lambda)$ and $b_b(\lambda)$ estimates are as high as 40% in the blue spectral region for $\mathrm{IOP}_{a\text{-}Chl}$ profiles [Figs. 2(f) and 2(g)].

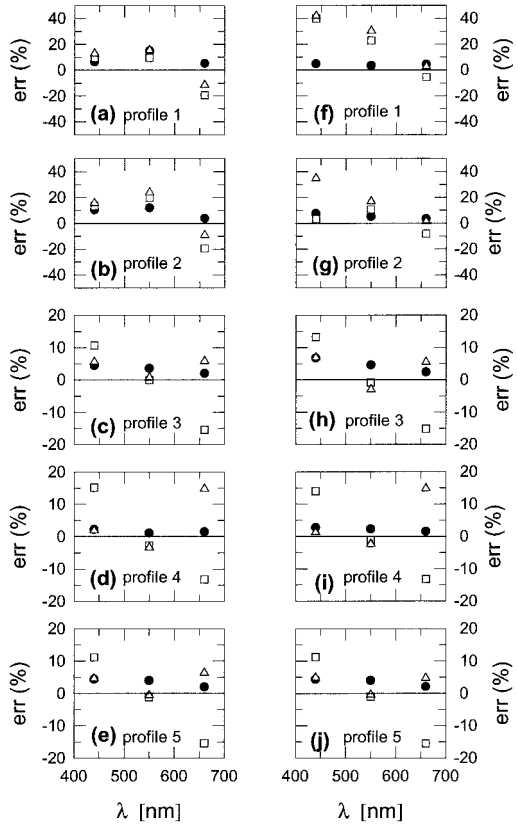

Fig. 2. Comparison of errors (in percent) in the values of absorption, scattering, and backscattering coefficients estimated from our model when the vertical profiles of IOPs are defined by the $\mathrm{IOP}_{ab\text{-}Chl}$ (left) or the $\mathrm{IOP}_{a\text{-}Chl}$ (right) models as described in the text. The errors are plotted for the three selected wavelengths, 440, 555, and 660 nm, for each chlorophyll profile from Fig. 1, as indicated: circles, errors for the absorption coefficient; squares, those for the scattering coefficient; triangles, those for the backscattering coefficient.

5. Closure between the Measured and the Modeled Inherent Optical Properties

A. Field Data

The spectral values of $R(\lambda, z = 0^-)$ and $\langle K_d(\lambda)\rangle_1$, which are used as inputs to our model, show significant differences between off-shore and near-shore CalCOFI stations (Fig. 3). The off-shore stations in the open ocean are characterized by the highest values of $R(\lambda, z = 0^-)$ and the lowest $\langle K_d(\lambda)\rangle_1$ in the blue region of the spectrum (open circles in Fig. 3). Also, $R(\lambda, z = 0^-)$ decreases greatly with wavelength across the entire spectrum, which is a typical feature of waters with low concentrations of suspended and dissolved materials. The surface chlorophyll a concentrations at these open-ocean stations varied between 0.1 and 0.25 mg m^{-3}. At the near-shore CalCOFI stations with *Chl* ranging from 0.4 to 2 mg m^{-3}, $R(\lambda, z = 0^-)$ shows relatively low values and little spectral variation in the blue [solid circles in Fig. 3(a)]. In this case the decrease in $R(\lambda, z = 0^-)$ becomes significant only as the wavelength increases from the green to the red spectral region. This pattern indicates that the near-shore stations have greater amounts of suspended and dissolved matter in seawater, which result in stronger absorption, particularly at blue wave bands [Fig. 4(a)], as well as stronger backscattering at all wavelengths [Fig. 4(b)]. This observation is also consistent with higher values of $\langle K_d(\lambda)\rangle_1$ in the blue, which increase with decreasing wavelength for the near-shore stations [Fig. 3(b)]. Figure 3 also shows data that represent intermediate cases (see triangles in Fig. 3) between the near-shore and the open-ocean stations.

The $R(\lambda, z = 0^-)$ and $\langle K_d(\lambda)\rangle_1$ spectra for near-shore COASTlOOC stations show even greater deviation from the clear-water patterns than the near-shore

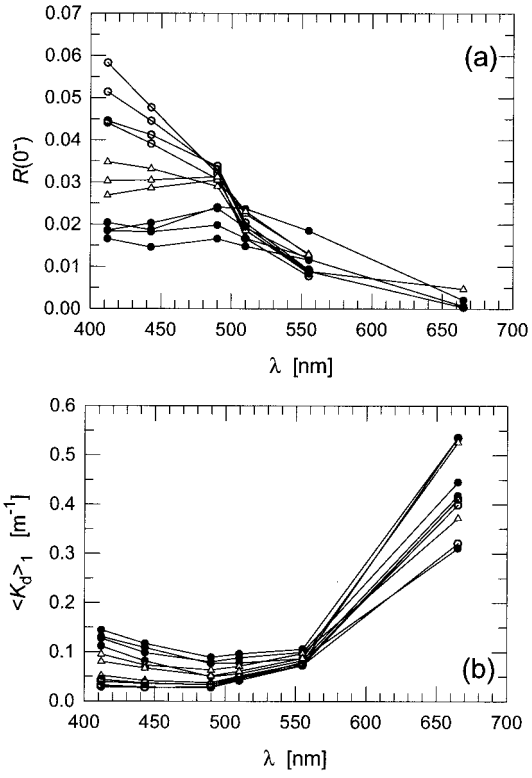

Fig. 3. (a) Spectral reflectance just beneath the sea surface and (b) the vertical attenuation coefficient for downwelling irradiance averaged within the first attenuation layer obtained from measurements at CalCOFI stations: Open and solid circles, data collected at off-shore and near-shore stations, respectively; triangles, spectral curves intermediate between the off-shore and the near-shore spectra.

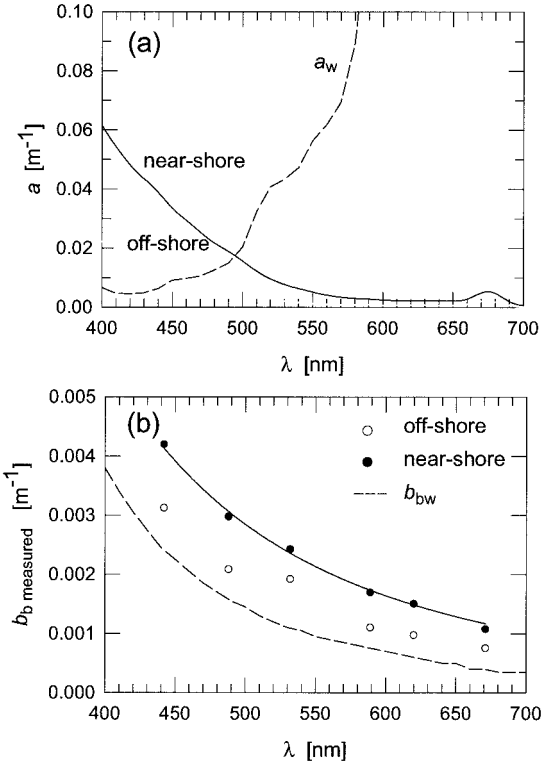

Fig. 4. Examples of the (a) measured spectral absorption coefficient and (b) the backscattering coefficient averaged within the first attenuation layer for off-shore and near-shore CalCOFI stations (see text for details about the measurements). These spectra correspond to the total absorption and backscattering coefficients after the contribution of pure seawater is subtracted. The pure seawater absorption and backscattering spectra are also shown for comparison (dashed curves). (b) The solid curves correspond to a power function fitted to measurements of backscattering at six wavebands, indicated by open and solid circles. The measurements of absorption were made with a high spectral resolution at 2-nm intervals.

CalCOFI stations. In areas strongly affected by discharge from the Rhone and Rhine Rivers, $R(\lambda, z = 0^-)$ shows a well-pronounced maximum in the green spectral band [see solid circles, Fig. 5(a)]. This maximum can be attributed to enhanced backscattering that is due to the high concentration of suspended particles and strong absorption in the blue by suspended and dissolved materials. In these turbid waters, $R(\lambda, z = 0^-)$ can reach values of greater than 0.04 in the green wave band, which is significantly greater than the corresponding values observed at other COASTlOOC and CalCOFI stations. Although a decrease in $R(\lambda, z = 0^-)$ toward the red portion of the spectrum is caused primarily by the increased absorption of pure seawater, a sharp decrease toward shorter wavelengths indicates that the Rhone and Rhine Rivers discharge large amounts of suspended and dissolved materials that absorb strongly in the blue. This absorption effect is also reflected in high values of $\langle K_d(\lambda)\rangle_1$ at short wavelengths [see solid circles, Fig. 5(b)].

The COASTlOOC data acquired in the Atlantic are characterized by a gradual decrease of $R(\lambda, z = 0^-)$ with increasing wavelength [open circles, Fig. 5(a)], which is generally representative of case 1 waters with low to moderate concentrations of phytoplankton and covarying materials. Because the surface concentration of chlorophyll a at these stations varied over a relatively wide range from 0.14 to 1.3 mg m^{-3}, $R(\lambda, z = 0^-)$ shows a correspondingly large variation in the blue spectral region. Similarly, $\langle K_d(\lambda)\rangle_1$ varies considerably at short wavelengths [see open circles, Fig. 5(b)]. The two remaining examples depicted in Fig. 5 (see triangles) represent the Mediterranean stations with little or no influence from Rhone River discharge. Therefore these stations resemble, to a certain extent, the open-ocean stations in the Atlantic with low *Chl*. One remarkable difference is that $R(\lambda, z = 0^-)$ in the green spectral region has higher values at the Mediterranean stations than in the Atlantic. This result suggests that the relative roles played by backscattering and absorption in controlling the reflectance are different in these two regions. The role of backscattering appears to be greater at the Mediterranean stations.

Two dimensionless quantities that involve IOPs, that is, b/a and η $(=b_w/b)$ ranging from 0 to 10 and from 0 to 0.2, respectively, were used in the development of our model.[1] These ranges are representa-

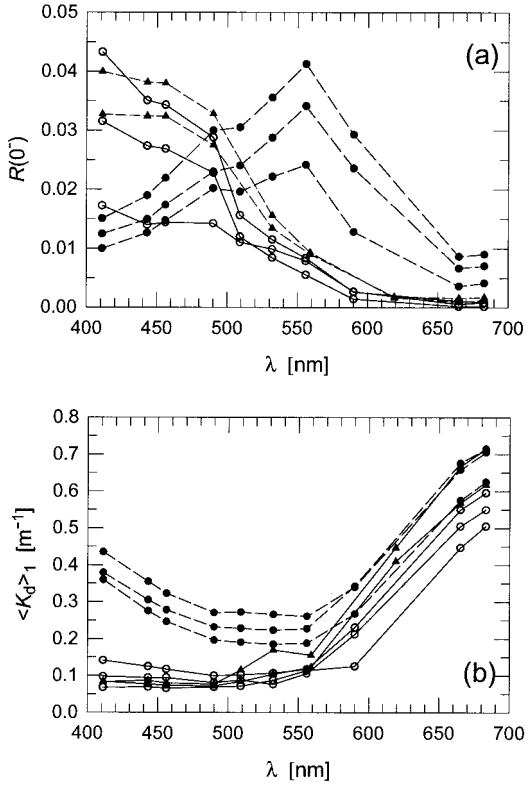

Fig. 5. (a) Spectral reflectance just beneath the sea surface and (b) the vertical attenuation coefficient for downwelling irradiance averaged within the first attenuation layer obtained from measurements at selected COASTlOOC stations: open circles, data collected in the Atlantic; solid circles, coastal waters affected by discharge from the Rhone and the Rhine Rivers; triangles, Mediterranean stations unaffected by the Rhone River discharge.

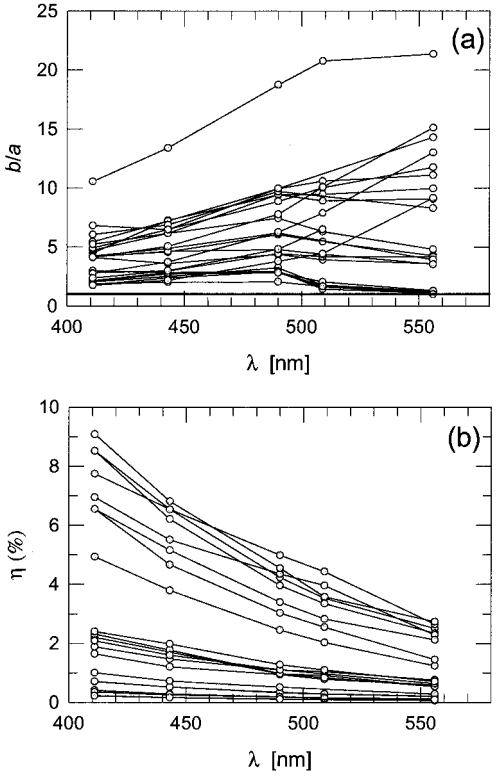

Fig. 6. Spectral values of (a) the scattering-to-absorption ratio and (b) the parameter η calculated from the COASTlOOC data.

tive of optical variability in most oceanic waters within the visible part of the spectrum and are consistent with ac-9 measurements at the COASTlOOC stations (Fig. 6). The data from ac-9 measurements are plotted for five spectral bands that match the wave bands available with the SPMR measurements of $R(\lambda, z = 0^-)$ and $\langle K_d(\lambda)\rangle_1$. The b/a ratio is generally less than 10, with the exception of one station in the immediate vicinity of the Rhine River mouth and several data points in the green collected at other stations in turbid waters [Fig. 6(a)]. Because b/a is always greater than 1, the scattering process dominates the beam attenuation for the illustrated set of data. The parameter η is significantly lower than the maximal value of 0.2 used in the development of the model, and it shows a decrease with wavelength. The distinctive set of curves with low values of η, generally below 0.02, represents coastal waters with relatively high turbidity.

B. Comparison of the Measured and Modeled Inherent Optical Properties

For a comparison of the measured and the modeled IOPs we use the average values of $a(\lambda, z)$, $b(\lambda, z)$, and $b_b(\lambda, z)$ obtained from measurements within the upper ocean down to the first attenuation depth. For the COASTlOOC stations these averages were calculated from vertical profiles of $a(\lambda, z)$ and $b(\lambda, z)$ obtained with ac-9. For the CalCOFI stations the averaging process was applied to the vertical profiles of $b_b(\lambda, z)$ obtained with Hydroscat-6 and to a few discrete depths for the absorption coefficient obtained with an onboard spectrophotometer. Because our model is not intended for low Sun positions, stations with θ_0 greater than 75° were excluded from the analysis. Although the model was developed for clear skies, some selected stations with overcast conditions are included in this analysis. At these overcast stations, θ_0 was ~50°. Radiative-transfer simulations show that for such a Sun position, our model can still be applied regardless of whether clouds are present.

Figure 7 shows that there is reasonably good closure between the modeled and the measured values of the absorption coefficient. If all CalCOFI and COASTlOOC absorption data including the considered wavelengths from the blue-green spectral region are pooled together and compared with the modeled estimates, the correlation is very high ($r^2 = 0.98$) [Fig. 7(a)]. The average value and the standard deviation of the relative difference between the measured and the modeled estimates are 14% and 11%, respectively. Note that this comparison is made for the absorption coefficient owing to the combined effects of particulate and dissolved materials after subtracting the contribution of pure water, $a - a_w$. (The subscript w is used to denote the contribution of pure seawater.) The values of $a - a_w$ cover a broad

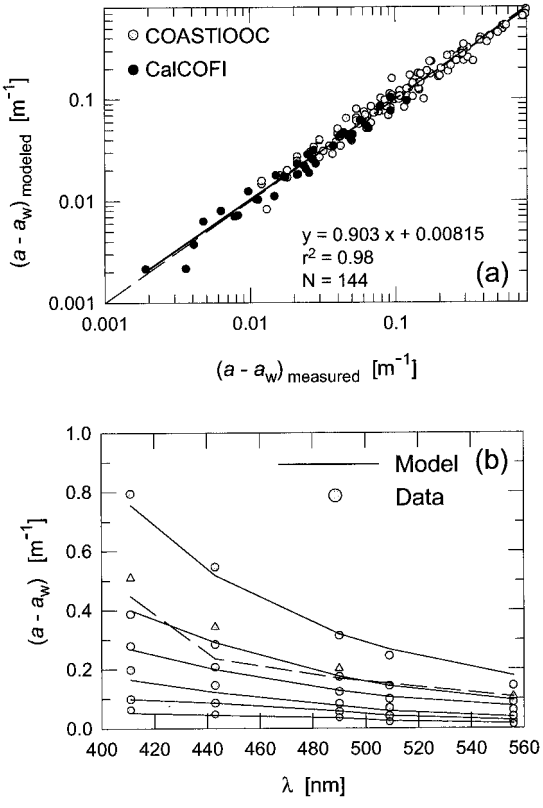

Fig. 7. (a) Comparison of the modeled and the measured absorption coefficients with the contribution of pure seawater subtracted. All data for the blue-green spectral wave bands from the CalCOFI and the COASTlOOC stations considered in this study are included: solid line, linear regression fit to the data points; dashed line, an ideal match between the measured and the modeled values. (b) Comparison of the modeled absorption spectra (solid lines) and the measured spectral absorption coefficients (circles, triangles) for selected stations. Dashed line, triangles, specific station in the Lions Gulf (see text for more details).

range from 0.002 to 0.8 m^{-1} with most data between 0.01 and 0.2 m^{-1}. The slope of this relationship differs slightly from the value of 1 that would represent the best match between the measured and the modeled values. One possible reason for the observed slope is the overestimation of the measured absorption coefficient that is due to the incomplete correction for the scattering error.[11,28] Other possibilities include errors in the measurements of light-field characteristics or a tendency of the model to underestimate absorption. In previous tests of the model with radiative-transfer simulations, no systematic bias in the absorption estimates was observed, however (see Fig. 7 in Ref. 1).

The spectra of the modeled and the measured absorption coefficients within the blue-green spectral region are compared for several stations in Fig. 7(b). In general there is good agreement between the model and the measurements. In some cases the discrepancies can be significant, especially at stations in the Lions Gulf [dashed curve in Fig. 7(b)]. At these stations the presence of a thin surface layer rich

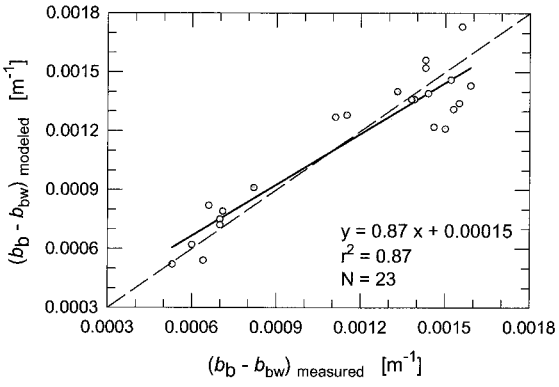

Fig. 8. Comparison of the modeled and the measured particle backscattering coefficient. All data for the blue-green wave bands and CalCOFI stations considered in this study are included: solid line, linear regression fit to the data points; dashed line, perfect match between the model and measurements.

in suspended particles can adversely affect the retrieval of the absorption coefficient from the model as shown in Fig. 2.

A reasonable closure is also achieved between the modeled and the measured values of the backscattering coefficient (Fig. 8). The comparison between the model and measurements is made for the particulate backscattering, $b_{bp} = b_b - b_{bw}$, where b_{bw} is taken as half of the scattering coefficient of pure seawater b_w.[26] Although the slope of the best fit to the data in Fig. 8 is less than 1, the relative differences between the modeled and the measured backscattering coefficients do not exceed 20% within the examined range of b_{bp} values. The average value and the standard deviation of the relative difference are 9.5% and 6%, respectively.

In contrast to the absorption and the backscattering coefficients, the differences between the modeled and the measured values of the scattering coefficient are typically large (Fig. 9). Even if the open-ocean stations in the Atlantic are considered as a separate subset of data, the closure for the particulate-scattering coefficient, $b_p = b - b_w$, is far from achieved [Fig. 9(b)]. The model estimates of b_p are generally much lower than the values obtained from measurements. Note that this discrepancy has no significant effect on the retrieval of b_b in this study, although b is involved in the estimation of b_b from Eq. (3). The effect of b on the retrieval of b_b can, however, be significant for large Sun zenith angles and high backscattering values (see Fig. 4 in Ref. 1). The observed bias between the modeled and the measured b_p is most likely associated with the effects of the scattering phase function of particles on the performance of the model. Our previous study showed that, although the retrievals of the absorption and backscattering coefficients from the model depend weakly on the particle phase function, estimates of the scattering coefficient are highly sensitive to variations in this function.[1] Therefore, assuming that the measurement errors are small, the results in Fig. 9 indicate that the actual particle phase functions at

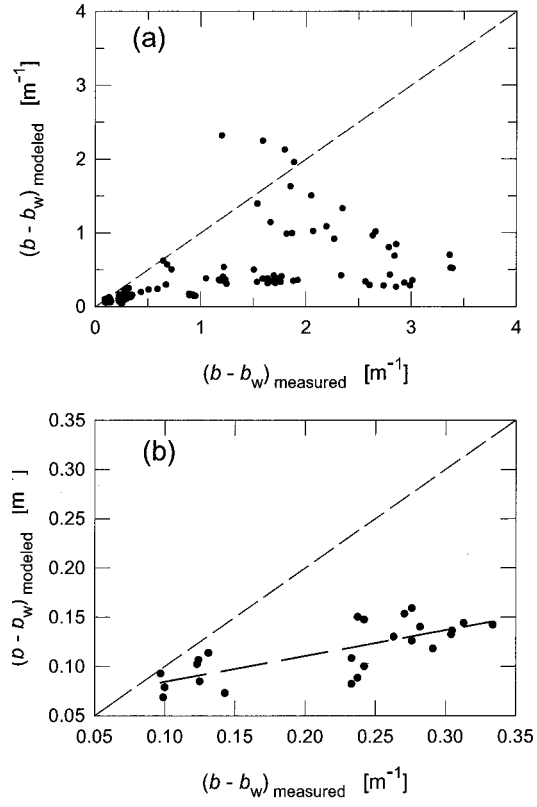

Fig. 9. (a) Comparison of the modeled and measured particle-scattering coefficient. All data for the blue-green wave bands and COASTlOOC stations considered in this study are included: short-dashed line, perfect match between the model and measurements. (b) As in (a), but the data points are only from the Atlantic: long-dashed line, short-dashed line, linear regression fit to the data points and the perfect agreement, respectively.

the COASTlOOC stations could differ significantly from the Petzold phase function used in the development of our model. The model-derived underestimates of b_p in Fig. 9 are similar to those observed earlier when the model was tested with a theoretical particle phase function representing a generic assemblage of marine organic particles (detritus) with a low refractive index (see Fig. 7 in Ref. 1). The backscattering ratio of the detritus phase function was 0.0054 compared with 0.019 for the Petzold function. Thus the data in Fig. 9 could suggest that the assemblages of suspended particles in the investigated waters exhibited a significantly lower probability of backscattering than that corresponding to the Petzold phase function. The ability to make such a hypothesis based on large discrepancies between the modeled and the measured b_p is itself a useful result of this closure analysis, especially because measurements of the scattering function are rare.

C. Estimation of $a(\lambda)$ and $b_b(\lambda)$ from $R(\lambda, z = 0^-)$

At a given solar zenith angle θ_0 our model normally requires $\langle K_d(\lambda)\rangle_1$ and $R(\lambda, z = 0^-)$ as input to the calculation of the IOP coefficients at wavelength λ. It is of particular interest, however, to examine the model when $R(\lambda, z = 0^-)$ is used as the only input besides θ_0. In this case $\langle K_d(\lambda)\rangle_1$ must be determined first from $R(\lambda, z = 0^-)$. Knowing both $\langle K_d(\lambda)\rangle_1$ and $R(\lambda, z = 0^-)$, we can then calculate the IOP coefficients from the equations of the model in a regular way. This particular application of the model provides the capability for retrieval of the IOPs from remotely sensed ocean color. This is because $R(\lambda, z = 0^-)$ is linked to the water-leaving radiance $L_w(\theta_v, \phi_v, \lambda, z = 0^+)$ in a fairly straightforward manner,[27] and $L_w(\theta_v, \phi_v, \lambda, z = 0^+)$ can in turn be derived from radiance measured by a remote sensor after contributions from light scattering in the atmosphere and sea surface reflection are corrected.[29,30] The zenith and azimuth angles, θ_v, ϕ_v, respectively, define the viewing direction from the point on the sea surface being examined by the sensor.

The relationship between $R(\lambda, z = 0^-)$ and $L_w(\theta_v, \phi_v, \lambda, z = 0^+)$ can be written as[27]

$$L_W(\theta_V, \phi_V, \lambda, z = 0^+) = \Re \frac{R(\lambda, z = 0^-)}{Q(\theta_V, \phi_V, \lambda, z = 0^-)} \times E_d(\lambda, z = 0^+), \quad (8)$$

where $\Re$ involves several quantities that account for the processes of reflection and refraction of light at the air–water interface and Q is the ratio of the upwelling plane irradiance $E_u(\lambda, z = 0^-)$ to the upwelling radiance $L_u(\theta_v', \phi_v', \lambda, z = 0^-)$ just beneath the surface at $z = 0^-$. The in-air and in-water zenith angles, θ_v and θ_v', respectively, are related by Snell's law, and the azimuth angles are the same in air and water, $\phi_v = \phi_v'$. For many remote-sensing experiments when θ_v and θ_v' are relatively small and $R(\lambda, z = 0^-) < 0.1$, a constant value of 0.54 is often assumed for the $\Re$ term.[31] The factor of Q generally ranges from 3 to 6 depending on direction, wavelength, water IOPs, and sky conditions. This factor can be estimated in case 1 waters from the procedure developed by Morel and Gentili.[32,33] The satellite sensor POLDER (polarization and directionality of the Earth's reflectances), which views one ground pixel at various angles,[34] can also provide the capability to estimate Q.

To estimate $\langle K_d(\lambda)\rangle_1$ from reflectance, we first use the empirical relationship developed by Mueller and Trees[35]:

$$\langle K_d(490)\rangle_1 = 0.022 + 0.1\left[\frac{L_{WN}(443)}{L_{WN}(555)}\right]^{-1.29966}, \quad (9)$$

where $L_{WN}(\lambda)$ is the normalized water-leaving radiance, which is approximately the water-leaving radiance that would exit the ocean toward the zenith in the absence of atmosphere with the Sun at the zenith.[30,36] $L_{WN}(\lambda)$ is related to $R(\lambda, z = 0^-)$ through

$$L_{WN}(\lambda) = \frac{F_0 \Re_n}{Q_n} R(\lambda, z = 0^-), \quad (10)$$

where F_0 is the mean extraterrestrial solar irradiance and $\Re_n$ and Q_n are the same variables as in Eq. (8), but in this case these values are calculated for the upwelling radiance with the direction of photon travel pointing toward the zenith and the Sun at the zenith. Combining Eqs. (9) and (10), we obtain

$$\langle K_d(490)\rangle_1 = 0.022 + 0.1 \times \left[\frac{R(443, z = 0^-)}{R(555, z = 0^-)} \frac{F_0(443)}{F_0(555)} \frac{\Re_n(443)}{\Re_n(555)} \frac{Q_n(555)}{Q_n(443)}\right]^{-1.29966}. \quad (11)$$

According to Neckel and Labs,[37] the ratio $F_0(443)/F_0(555)$ is 1.045. The spectral ratios of $\Re_n$ and Q_n can also be assumed to be close to 1. For example, the radiative-transfer simulations for chlorophyll concentrations ranging from 0.01 to 10 mg m^{-3} and the Sun zenith angle of 30° show that the ratio $Q_n(555)/Q_n(443)$ varies to within 3% in the vicinity of 1. To a satisfactory approximation, we can thus rewrite Eq. (9) by using a ratio of irradiance reflectance instead of the normalized water-leaving radiance,

$$\langle K_d(490)\rangle_1 = 0.022 + 0.1\left[\frac{R(443, z = 0^-)}{R(555, z = 0^-)}\right]^{-1.29966}, \quad (12)$$

and we use Eq. (12) to calculate $\langle K_d(490)\rangle_1$. Note that the $\langle K_d(490)\rangle_1$ estimate is independent of the value of the reflectance at 490 nm. Knowing $\langle K_d(490)\rangle_1$ and $R(490, z = 0^-)$, we can now apply our model in a regular way to retrieve a and b_b at 490 nm.

The next step is to calculate the spectral values of $\langle K_d(\lambda)\rangle_1$ from empirical relationships that relate $\langle K_d(\lambda)\rangle_1$ at a given wavelength λ to $\langle K_d(490)\rangle_1$. These relationships have the general form

$$\langle K_d(\lambda)\rangle_1 = A(\lambda)\langle K_d(490)\rangle_1 + B(\lambda), \quad (13)$$

where the coefficients $A(\lambda)$ and $B(\lambda)$ are determined from observations. We use the values of $A(\lambda)$ and $B(\lambda)$ established by Austin and Petzold[38] in the blue spectral region at λ = 410 and 440 nm and those of Kishino *et al.*[39] at 510 and 555 nm. [This combination provides the best retrieval of $\langle K_d(\lambda)\rangle_1$ for the present set of data.] Note that these wavelengths can represent a shift of a few nanometers compared with the nominal wavelengths in our radiometric measurements with MER-2048 and SPMR. This shift is negligible because the half-bandwidth in the spectral measurements is ~10 nm. The spectral values of $\langle K_d(\lambda)\rangle_1$ calculated from our measurements of reflectance by using Eqs. (12) and (13) agree well with direct determinations of $\langle K_d(\lambda)\rangle_1$ from our measurements at CalCOFI and COASTlOOC stations (Fig. 10).

Having determined $\langle K_d(\lambda)\rangle_1$ from Eqs. (12) and (13), we can now use the model of Eqs. (1)–(5) to calculate the absorption and the backscattering coefficients and compare these estimates with the values determined from measurements (Fig. 11). The modeled and measured values of the absorption coefficient, $a - a_w$, still show a significant correlation [Fig. 11(a)]. However, compared with the case when both inputs to the model, $R(\lambda, z = 0^-)$ and $\langle K_d(\lambda)\rangle_1$, are obtained from measurements [see Fig. 7(a)], the squared correlation is reduced from 0.95 to 0.75. Also, the slope of the relationship between the modeled and the measured values is reduced significantly below the value of 1. The intercept of the regression is greater in Fig. 11(a) than in Fig. 7(a). Note that the value of the intercept in Fig. 11(a) is similar to that for the $\langle K_d(\lambda)\rangle_{1\ \text{modeled}}$ versus $\langle K_d(\lambda)\rangle_{1\ \text{measured}}$ relationship in Fig. 10. Nevertheless Fig. 11(a) demonstrates that the agreement between the modeled and the measured absorption coefficient is generally good when $R(\lambda, z = 0^-)$ is used as the only measured input to the model. In this case, the average value and the standard deviation of the relative difference between the measured and the model values are 26% and 16%, respectively.

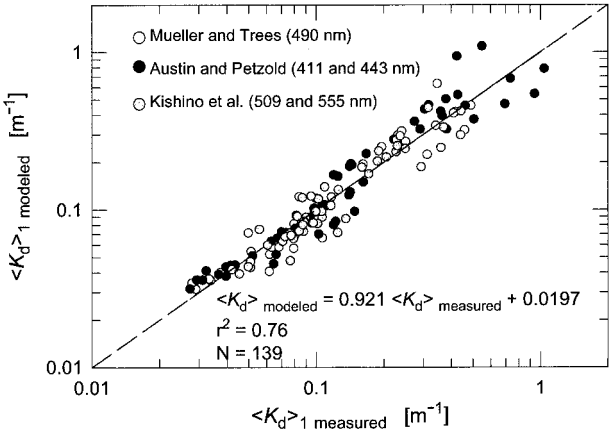

Fig. 10. Estimates of the vertical attenuation coefficient of downwelling irradiance from the three empirical models plotted versus the values from our *in situ* measurements at the CalCOFI and the COASTlOOC stations. The different symbols represent the various empirical models used for specific wavelengths, as indicated: dashed line, perfect agreement between the model and observations; solid line, linear regression fit to the data points. The standard errors of the slope and intercept of the regression are 0.0447 and 0.0112, respectively.

In a similar way the results for the backscattering coefficient b_{bp} are compared in Fig. 11(b). The slope of the relationship between the modeled and the measured values is 0.7, which is less than the slope shown in Fig. 8 for the case in which both inputs to the model, $R(\lambda, z = 0^-)$ and $\langle K_d(\lambda)\rangle_1$, were taken from measurements. The squared correlation coefficient remains almost unchanged (0.81), but the intercept parameter increased by 40%. However, the relative difference between the modeled and the measured b_{bp} never exceeds 30%, which is similar to the results in Fig. 8. The average value for this difference in Fig. 11(b) is 17% (10% for the standard deviation) compared with 9.5% in Fig. 8. We can conclude that the use of the estimated values of $\langle K_d(\lambda)\rangle_1$ from Eqs. (12) and (13) instead of measured $\langle K_d(\lambda)\rangle_1$ has a relatively small effect on the overall agreement between

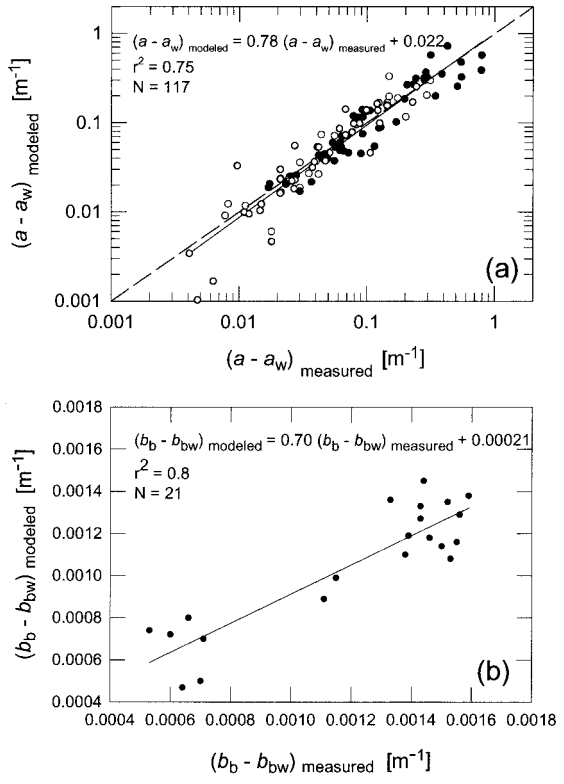

Fig. 11. (a) Comparison of the modeled and the measured absorption coefficient for a special case in which the reflectance just beneath the sea surface is the only measurement used as input to the model (see text for more details): solid, dashed lines, linear regression fit and the perfect agreement, respectively. The standard errors of the slope and the intercept parameters of the regression are 0.0431 and 0.0081, respectively. Note that the number of data points in (a), which were obtained during the CalCOFI and the COASTlOOC experiments, is not the same as in Fig. 7(a) because the measurements of $R(z = 0^-)$ at 443 and 555 nm necessary to calculate $\langle K_d(490)\rangle_1$ were not available at all stations. (b) As in (a) but for the backscattering coefficient (recall that the measurements of backscattering are from CalCOFI stations only).

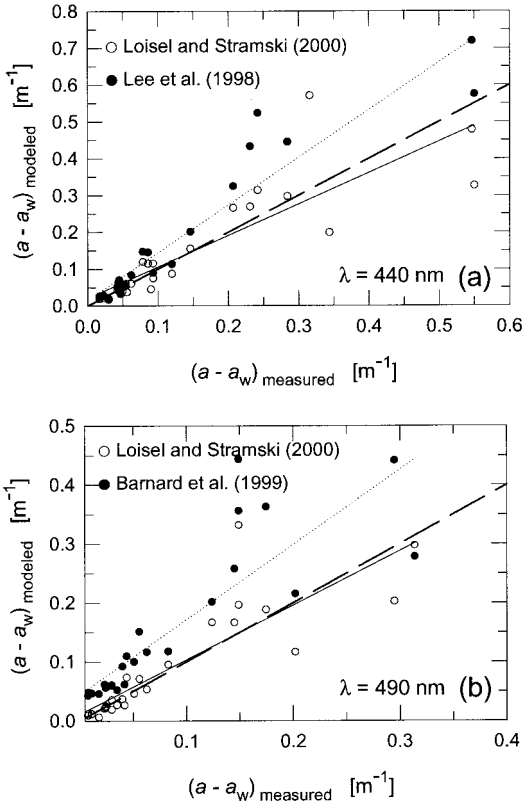

Fig. 12. Comparison of the modeled and the measured absorption coefficients at two specific wavelengths: (a) $\lambda = 440$ nm; (b) $\lambda = 490$ nm. For each wavelength, two different models are compared with measurements, as indicated: dashed line, perfect agreement between the model and observations. The linear regression fit to the data points, solid line, for our model and, dotted line, for the two other models (Lee *et al.* at $\lambda = 440$ nm, and Barnard *et al.* at $\lambda = 490$ nm).

the modeled and the measured values of the backscattering coefficient.

D. Comparison of Various Models for Retrieving $a(\lambda)$

In recent years significant efforts have been devoted to the development of models for retrieving the absorption coefficient from remote-sensing reflectance R_{rs}, which is defined as the ratio of the water-leaving radiance to the downwelling irradiance just above the sea surface.[6,7,40–42] Some models, referred to as empirical models, are simply based on the regression analysis applied to observations (see, e.g., Ref. 6). Other models, often referred to as semianalytical models, are typically based on the general relationship between the reflectance and the backscattering-to-absorption ratio and some empirical parameterizations or relationships (see, e.g., Refs. 7 and 42). Our model belongs to yet another class of model in which all equations used in the estimation of IOPs are developed from radiative-transfer simulations for a broad range of environmental conditions. One can expect that the performance of the different types of model will differ because the assumptions and sources of uncertainties are not the same. Below we compare the retrieval of the absorption coefficient from the three models, the empirical model of Lee *et al.*,[6] the semianalytical model of Barnard *et al.*,[7] and our model, with absorption measurements taken at CalCOFI and COASTlOOC stations.

The algorithm of Lee *et al.* is based on data from open ocean and coastal waters and utilizes one or two spectral ratios of R_{rs} as part of empirically derived nonlinear relationships to estimate the total absorption coefficient at 440 nm. The three-band algorithm involving a combination of two spectral ratios, $R_{rs}(440)/R_{rs}(555)$ and $R_{rs}(490)/R_{rs}(555)$, was suggested to provide the best retrieval, and therefore it is used for the present comparison. The algorithm of Barnard *et al.* employs two spectral ratios of R_{rs} at three wavelengths (443, 490, and 555 nm) to estimate the total absorption coefficient at 490 nm from a semianalytical approach. This approach takes advantage of the fact that the influences of the angular distribution of light and the backscattering coefficient on the resultant triple reflectance ratio are

Table 2. Parameters of the Linear Regression Analysis Between the Modeled and the Measured Absorption Coefficients[a]

Predicted Versus Measured Absorption	Slope	Offset	r^2
$a(440)$, Ref. 1	0.852 (0.103)	0.0205 (0.0216)	0.75
$a(440)$, Ref. 6	1.294 (0.100)	0.0148 (0.0210)	0.85
$a(490)$, Ref. 1	0.925 (0.115)	0.0110 (0.0138)	0.74
$a(490)$, Ref. 7	1.273 (0.164)	0.0443 (0.0198)	0.72

[a]The standard error of each parameter is in parentheses.

greatly reduced. Empirical relationships between the absorption at 490 nm and other wavelengths[43] are involved in the algorithm. These relationships were developed from data collected in open ocean and coastal waters. Although these two models were developed in terms of spectral ratios of R_{rs}, they can also be applied if $R(\lambda, z = 0^-)$ is used as input instead of R_{rs}. Because R_{rs} and R are related through $R_{rs} = \Re R/Q$, and both $\Re$ and Q are expected to show weak wavelength dependence (see discussion above), the spectral ratios of R_{rs} are expected to be similar to the corresponding ratios of R. To ensure consistency in the comparison of models and observations, we use the appropriate spectral ratios of R as input to the models of Lee *et al.*[6] and Barnard *et al.*,[7] and the values of R at a single wavelength are examined as input to our model.

The models of Lee *et al.* and Barnard *et al.* show a tendency to overpredict the absorption coefficient, $a - a_w$, if compared with the estimates from measurements (Fig. 12). For the Lee *et al.* model this tendency is clearly seen at higher absorption values [Fig. 12(a)]. In contrast our model shows no systematic departure from measurements, or perhaps only a slight underprediction, although data points are significantly scattered, especially when $a - a_w$ is high. Note that we have chosen to illustrate the results for 440 nm in the case of the Lee *et al.* model [Fig. 12(a)] and 490 nm in the case of the Barnard *et al.* model [Fig. 12(b)], because these models were developed for these particular wavelengths. The parameters of the linear regression analysis between the modeled and the measured absorption coefficients from Fig. 12 are displayed in Table 2. These parameters indicate that our model provides generally better agreement with measurements than the other two models. The result that the models of Lee *et al.* and Barnard *et al.* yield estimates that are often significantly higher than the measured values is consistent with a comparison with a different data set from the Gulf of California and Northeast Atlantic Shelf presented by Barnard *et al.*[7]

5. Conclusions

We previously developed an inverse model to retrieve $a(\lambda)$, $b(\lambda)$, and $b_b(\lambda)$ within the upper ocean from two basic apparent optical properties, $R(\lambda, z = 0^-)$ and $\langle K_d(\lambda)\rangle_1$.[1] We have tested the performance of this model in the present study by using measurements of a, b, and b_b made simultaneously (or nearly simultaneously) with the radiometric measurements of the downwelling and upwelling plane irradiances. The data were collected in both the nearshore and off-shore marine environments during CalCOFI cruises off southern California and the COASTlOOC experiment in waters surrounding Europe. A broad range of water optical properties from clear case 1 waters to sediment-dominated and yellow substance-dominated case 2 waters was included in these measurements.

The comparison between the modeled and the measured absorption and backscattering coefficients shows generally good agreement for most environmental conditions experienced during the field experiments. An exception when the model performance was significantly degraded was found when there is a strong stratification of the optical properties in the near-surface layer. Nevertheless for most oceanic situations the model offers a robust tool for estimating $a(\lambda)$ and $b_b(\lambda)$ from measurements of $R(\lambda, z = 0^-)$ and $\langle K_d(\lambda)\rangle_1$.

The estimation of $b(\lambda)$ from our model is subject to much greater uncertainty than the retrieval of $a(\lambda)$ and $b_b(\lambda)$, which is related to the effect of the particle-scattering phase function. Compared with the *in situ* measurements with the ac-9 instrument, the model largely underestimates the particle-scattering coefficient $b_p(\lambda)$ at COASTlOOC stations. Assuming that the measurement errors are small, this result suggests that the actual particle phase functions in the examined waters differed significantly from the Petzold phase function that was used in the development of our model. We have shown that the use of a particle phase function with lower probability of backscattering than that of the Petzold function would provide a better agreement between the modeled and the measured $b_p(\lambda)$. This result itself is interesting because it indicates that a large systematic difference between the modeled and the measured $b_p(\lambda)$ can provide information about the general shape of the scattering function, which is rarely measured.

One obvious application of our model is when measurements of IOPs are not available. Another important application is for verifying the consistency between the IOP and the AOP measurements and the quality control of these measurements. The evaluation of accuracy and procedures to determine IOPs and AOPs from measurements remains an important challenge. For example, the absorption estimates from the ac-9 measurements are subject to the potential error associated with the residual scattering correction.[11,28] This correction can be difficult to achieve accurately, especially in turbid waters where scattering is strong and its angular properties are unknown. Uncertainty also continues regarding path-length amplification factors for $a_p(\lambda)$ determined with the filter-pad method. In a similar way, the determination of $b_b(\lambda)$ from Hydroscat-6 is not direct, because this instrument measures scattered intensity within a relatively narrow range of scattering angles near 140°, which is then used to estimate

$b_b(\lambda)$.[15] Thus attempts to understand discrepancies of closure between measurements and models continues to be important.

We have also tested the model within the context of the potential application to remote sensing. In this case the only measured apparent optical property used as input to the model is the irradiance reflectance $R(\lambda, z = 0^-)$. The other apparent property $\langle K_d(\lambda)\rangle_1$ is derived from reflectance when empirical relationships are used. Our model equations are then applied to estimating $a(\lambda)$ and $b_b(\lambda)$. Such an analysis showed that the model still provides reasonable values of $a(\lambda)$ and $b_b(\lambda)$, although the quality of retrieval appears to be reduced compared with the original model when both input AOPs, $R(\lambda, z = 0^-)$ and $\langle K_d(\lambda)\rangle_1$, are taken directly from measurements. Nevertheless these results are encouraging because they suggest the potential to derive information about the distribution of inherent optical properties in the surface ocean from the satellite imagery of ocean color.

This research was supported by the Environmental Optics Program of the U.S. Office of Naval Research (grant N00014-98-1-0003). Support for the CalCOFI data was provided by the U.S. Office of Naval Research (N00014-98-1-0247) and the NASA Sensor Intercomparison and Merger for Biological and Interdisciplinary Oceanic Studies (SIMBIOS) project contract NAS5-97130. Support for COASTlOOC data were provided by the European Commission program Environment and Climate (contract ENV4-CT96-0310). We acknowledge the crew of the R.V. Victor Hensen and R.V. Théthys II. We are grateful to G. Obolensky for help in collecting data and D. Doxaran for assistance with data processing. We especially thank M. Wernand for the loan of ac-9. The ship time was made available by the Centre National de la Recherche Scientifique (Paris) and Institut National des Sciences de l'Univers for the Thétys II, by Reedereigemeinschaft Forschungsschiffahrt GmgH for the R.V. Victor Hensen. Ship time for the CalCOFI cruises was supported by the University of California at San Diego and National Oceanic and Atmospheric Administration.

References

1. H. Loisel and D. Stramski, "Estimation of the inherent optical properties of natural waters from irradiance attenuation coefficient and reflectance in the presence of Raman scattering," Appl. Opt. **39,** 3001–3011 (2000).
2. H. R. Gordon, "Absorption and scattering estimates from irradiance measurements: Monte Carlo simulations," Limnol. Oceanogr. **36,** 769–777 (1991).
3. J. T. O. Kirk, "Estimation of the absorption and scattering coefficient of natural waters by use underwater irradiance measurements," Appl. Opt. **33,** 3276–3278 (1994).
4. C. S. Roesler and M. J. Perry, "*In situ* phytoplankton absorption, fluorescence emission, and particulate backscattering spectra determined from reflectance," J. Geophys. Res. **100,** 13,274–13,294 (1995).
5. H. R. Gordon and G. C. Boynton, "Radiance-irradiance inversion algorithm for estimating the absorption and backscattering coefficients of natural waters: homogeneous waters," Appl. Opt. **36,** 2636–2641 (1997).
6. Z. P. Lee, K. L. Carder, R. G. Steward, T. G. Peacock, C. O. Davis, and J. S. Patch, "An empirical ocean color algorithm for light absorption coefficients of optically deep waters," J. Geophys. Res. **103,** 27,967–27,978 (1998).
7. A. H. Barnard, J. R. V. Zaneveld, and W. S. Pegau, "*In situ* determination of the remotely sensed reflectance and the absorption coefficient: closure and inversion," Appl. Opt. **38,** 5108–5117 (1999).
8. M. Stramska, D. Stramski, B. G. Mitchell, and C. D. Mobley, "Estimation of the absorption and backscattering coefficients from in-water radiometric measurements," Limnol. Oceanogr. **45,** 628–641 (2000).
9. R. A. Leathers, C. S. Roesler, and N. J. McCornick, "Ocean inherent optical property determination from in-water light field measurements," Appl. Opt. **38,** 5096–5103 (1998).
10. H. R. Gordon and G. C. Boynton, "Radiance-irradiance inversion algorithm for estimating the absorption and backscattering coefficients of natural waters: vertically stratified water bodies," Appl. Opt. **37,** 3886–3896 (1998).
11. A. Bricaud, C. Roesler, and J. R. V. Zaneveld, "*In situ* methods for measuring the inherent optical properties of ocean waters," Limnol. Oceanogr. **40,** 393–410 (1995).
12. M. Sydor and R. A. Arnone, "Effects of suspended particulate and dissolved organic matter on remote sensing of coastal and riverine waters," Appl. Opt. **36,** 6905–6912 (1997).
13. J. A. Barth and D. J. Bogucki, "Spectral light absorption and attenuation measurements from a towed undulating vehicle," Deep Sea Res. **47,** 323–342 (2000).
14. H. Claustre, F. Fell, K. Oubelkheir, L. Prieur, A. Sciandra, B. Gentili, and M. Babin, "Continuous monitoring of surface optical properties across a geostrophic front: biogeochemical inferences," Limnol. Oceanogr. **45,** 309–421 (2000).
15. R. A. Maffione and D. R. Dana, "Recent measurements of the spectral backward scattering coefficient in coastal waters," in *Ocean Optics XIII*, S. G. Ackleson, ed., Proc. SPIE **2963,** 154–159 (1996).
16. B. G. Mitchell and M. Kahru, "Algorithms for Sea WIFS developed with the CalCOFI data set," CalCOFI Rep. 39 (CalFOFI, La Jolla, Calif., 1998).
17. R. M. Pope and E. S. Fry, "Absorption spectrum (380–700 nm) of pure water. II. Integrating cavity measurements," Appl. Opt. **36,** 8710–8723 (1997).
18. B. G. Mitchell, "Algorithm for determining the absorption coefficient of aquatic particulate using the quantitative filter technique (QFT)," in *Ocean Optics X*, R. W. Spinrad, ed., Proc. SPIE **1302,** 137–148 (1990).
19. A. Bricaud, A. Morel, and L. Prieur, "Absorption by dissolved organic matter of the sea (yellow substance) in the UV and visible domains," Limnol. Oceanogr. **26,** 43–53 (1981).
20. C. D. Mobley, *Hydrolight 4.0 User's Guide* (Sequoia Scientific, Mercer Island, Wash., 1998).
21. M. R. Lewis, J. J. Cullen, and T. Platt, "Phytoplankton and thermal structure in the upper ocean: consequences of nonuniformity in chlorophyll profile," J. Geophys. Res. **88,** 2565–2570 (1983).
22. T. Platt, S. Sathyendranath, C. M. Caverhill, and M. R. Lewis, "Ocean primary production and available light: further algorithms for remote sensing," Deep-Sea Res. **35,** 855–879 (1988).
23. A. Morel and B. Gentili, "Diffuse reflectance of oceanic waters: Its dependence on Sun angles as influenced by the molecular scattering contribution," Appl. Opt. **30,** 4427–4438 (1991).
24. H. Loisel and A. Morel, "Light scattering and chlorophyll concentration in case 1 waters: a reexamination," Limnol. Oceanogr. **43,** 847–858 (1998).
25. J. C. Kitchen and J. R. V. Zaneveld, "On the noncorrelation of

the vertical structure of light scattering and chlorophyll a in case 1 waters," J. Geophys. Res. **95,** 20,237–20,246 (1990).
26. A. Morel, "Optical properties of pure water and pure seawater," in *Optical Aspects of Oceanography*, N. G. Jerlov and E. Steeman Nielsen, eds. (Academic, London, 1974), pp. 1–24.
27. C. D. Mobley, *Light and Water: Radiative Transfer in Natural Waters* (Academic, San Diego, Calif., 1994).
28. J. R. V. Zaneveld, J. C. Kitchen, and C. C. Moore, "Scattering error correction of the reflecting tube absorption meter," in *Ocean Optics XII*, J. S. Jaffe, ed., Proc. SPIE **2258,** 44–55 (1994).
29. H. R. Gordon, "Removal of atmospheric effects from satellite imagery of the oceans," Appl. Opt. **17,** 1631–1636 (1978).
30. H. R. Gordon, "Atmospheric correction of ocean color imagery in the Earth Observing System era," J. Geophys. Res. **102,** 17,081–17,106 (1997).
31. R. W. Austin, "The remote sensing of spectral radiance from below the ocean surface," in *Optical Aspects of Oceanography*, N. G. Jerlov and E. Steeman Nielsen, eds. (Academic, London, 1974), pp. 317–344.
32. A. Morel and B. Gentili, "Diffuse reflectance of oceanic waters. II. Bidirectional aspects," Appl. Opt. **32,** 6864–6879 (1993).
33. A. Morel and B. Gentili, "Diffuse reflectance of oceanic waters. III. Implication of bidirectionality for the remote-sensing problem," Appl. Opt. **35,** 4850–4862 (1996).
34. P. Y. Deschamps, F. M. Breon, M. Leroy, A. Podaire, A. Bricaud, J. C. Buriez, and G. Seze, "The POLDER mission: instrument characteristics and scientific objectives," IEEE Trans. Geosci. Remote Sens. **32,** 598–615 (1994).
35. J. L. Mueller and C. Trees, "Revised Sea WIFS prelaunch algorithm for diffuse attenuation coefficient K(490)," Sea WIFS Technical Report Series, Nasa Tech. Memo. 104566, Vol. **41,** S. B. Hooker and E. R. Firestone, eds. (NASA Goddard Space Flight Center, Greenbelt, Md., 1997), pp. 18–21.
36. H. R. Gordon and D. K. Clark, "Clear water radiances for atmospheric correction of Coastal Zone Color Scanner imagery," Appl. Opt. **16,** 2257–2260 (1977).
37. H. Neckel and D. Labs, "The solar radiation between 3300 and 12500 Å," Solar Phys. **90,** 205–258 (1984).
38. R. W. Austin and T. J. Petzold, "The determination of the diffuse attenuation coefficient of sea water using the Coastal Zone Color Scanner," in *Oceanography from Space*, J. F. R. Gower, ed. (Plenum, New York, 1981), pp. 239–256.
39. M. Kishino, J. Ishizaka, H. Satoh, K. Kusaka, S. Saitoh, T. Miyoi, and K. Kawasaki, "Optical characteristics of sea water in the north Pacific ocean," in *Ocean Optics XIII*, S. G. Ackleson and R. Frouin, eds., Proc. SPIE **2963,** 173–178 (1996).
40. F. E. Hoge and P. E. Lyon, "Satellite retrieval of inherent optical properties by linear inversion of oceanic radiance models: an analysis of model and radiance measurement errors," J. Geophys. Res. **101,** 16,631–16,648 (1996).
41. M. Sydor, R. A. Arnone, R. W. Gould, Jr., G. E. Terrie, S. D. Ladner, and C. G. Wood, "Remote-sensing technique for determination of the volume absorption coefficient of turbid water," Appl. Opt. **37,** 4944–4950 (1998).
42. K. L. Carder, F. R. Chen, Z. P. Lee, and S. Hawes, "Semianalytic modis algorithms for chlorophyll-a and absorption with bio-optical domains based on nitrate-depletion temperatures," J. Geophys. Res. **104,** 5403–5421 (1999).
43. A. H. Barnard, W. S. Pegau, and J. R. V. Zaneveld, "Global relationships of the inherent optical properties of the oceans," J. Geophys. Res. **103,** 24,955–24,968 (1998).